BNL-113227-2016-JA

Biaxially Strained PtPb/Pt Core/Shell Nanoplate Boosts Oxygen Reduction Catalysis

Lingzheng Bu, Nan Zhang, Shaojun Guo, Xu Zhang, Jing Li, Jianlin Yao, Tao Wu, Gang Lu, Jing-Yuan Ma, Dong Su, and Xiaoqing Huang

Submitted to Science

December 2016

Center for Functional Nanomaterials

Brookhaven National Laboratory

U.S. Department of Energy
USDOE Office of Science (SC),
Basic Energy Sciences (SC-22)

DISCLAIMER

Biaxially Strained PtPb/Pt Core/Shell Nanoplate Boosts Oxygen Reduction Catalysis

Lingzheng Bu,[1] Nan Zhang,[1] Shaojun Guo,[2,3,4*] Xu Zhang,[5] Jing Li,[6] Jianlin Yao,[1] Tao Wu,[1] Gang Lu,[5] Jing-Yuan Ma,[7] Dong Su,[6*] and Xiaoqing Huang[1*] [1]College of Chemistry, Chemical Engineering and Materials Science, Soochow University, Jiangsu 215123, China. [2]Department of Materials Science & Engineering, &Department of Energy and Resources Engineering, College of Engineering, Peking University, Beijing 100871, China. [3]BIC-ESAT, College of Engineering, Peking University, Beijing 100871, China. [4]Key Laboratory of Theory and Technology of Advanced Batteries Materials, College of Engineering, Peking University, Beijing 100871, China. [5]Department of Physics & Astronomy, California State University, Northridge, California 91330, USA. [6]Center for Functional Nanomaterials, Brookhaven National Laboratory, Upton, New York 11973, USA. [7]Shanghai Synchrotron Radiation Facility, Shanghai Institute of Applied Physics, Chinese Academy of Sciences, Shanghai 201204, China. *To whom correspondence should be addressed. E-mail: guosj@pku.edu.cn; dsu@bnl.gov; hxq006@suda.edu.cn

Compressive surface strains have been necessary to boost oxygen reduction reaction (ORR) activity in core/shell M/Pt catalysts (where M can be Ni, Co, Fe), we report a class of PtPb/Pt core/shell nanoplate catalysts that exhibit large biaxial tensile strains. The stable Pt (110) facets of the nanoplates have high ORR specific and mass activities that reach 7.8 milliampere per centimeter square and 4.3 ampere per milligram of platinum at 0.9 volts versus the reversible hydrogen electrode (RHE), respectively. Density functional theory calculations revealed that the edge-Pt and top (bottom)-Pt (110) facets undergo large tensile strains that help optimize the Pt-O bond strength. The intermetallic core and uniform 4 layers of Pt shell of the PtPb/Pt nanoplates appear to underlie the high endurance of these catalysts, which can undergo 50,000 voltage cycles with negligible activity decay and no apparent structure and composition changes.

Nanostructured platinum (Pt) is efficient catalyst for fuel cells as well as various industrial chemical reactions (1-4), but its high cost impedes its large-scale commercialization (5-7). The most successful catalysts for boosting the activity of catalysts for the oxygen reduction reaction (ORR) on a per-Pt-atom basis have been PtM alloy nanoparticles (NPs) (where M has been Ni, Co, Fe, among other metals) with a Pt-skin surface (core-shell structure). However, the formation of either a disordered PtM core or non-uniform Pt-skin layer (8-14) usually results in poor electrocatalytic stability after long-term voltage cycling.

In general, tuning or optimizing the oxygen adsorption energy through adjusting the compressive strain of the Pt surface is believed an effective approach to improve the ORR activity (15, 16). Ordered intermetallic phases with high 3d transition metal content can be used to provide better control over the compressive strain effect for optimized catalysis (17). The optimal compressive strain to Pt(111) facet in PtM/Pt core/shell NPs is particularly necessary for boosting ORR catalysis. The tensile strain on the Pt(111) facet is usually believed undesirable because such surface strain will result in overly strong binding of the oxygen species to the surfaces during the catalysis process. Although the activity enhancement has been demonstrated in the core/shell electrocatalyst with a Pt monolayer shell (causing limited durability) and an intermetallic PtPb core (18), the control over the stable and active facets of Pt shell onto PtPb core, and the investigation of strong tensile strain for ORR enhancement have not been explored.

We report a class of highly uniform PtPb/Pt core/shell nanoplates with large biaxial tensile strain for boosting ORR. Rather than use compressive strain to optimize the oxygen adsorption energy, we show that at a very high tensile strain, the Pt(110) plane located outside the nanoplates can exhibit the superior electrocatalytic activity for ORR (19, 20). By integrating the strong tensile strain of PtPb to Pt(110) facet along [100] direction with thin two-dimensional (2D) morphology and intermetallic phase (ensuring high chemical stability), the as-prepared nanoplate can deliver specific and mass activities for ORR that are 33.9 and 26.9 times greater than those of the commercial Pt/C catalyst (8, 21, 22). The PtPb nanoplates show negligible activity decay and no obvious structure and composition changes after a 50,000-cycle electrochemical accelerated durability test (ADT). They are also extremely active and stable for anodic oxidation reactions, largely outperforming those based on the PtPb NPs and the commercial Pt/C in both methanol oxidation reaction (MOR) and ethanol oxidation reaction (EOR).

We synthesized PtPb/Pt core/shell hexagonal nanoplates in nonaqueous conditions using platinum (II) acetylacetonate ($Pt(acac)_2$) and lead (II) acetylacetonate ($Pb(acac)_2$) as the metal precursors, oleylamine (OAm)/octadecene (ODE) mixture as solvents and surfactants, and ascorbic acid (AA) as the reducing agent [details in supporting information (SI) (23)]. The structure of nanoplates was characterized by transmission electron microscopy (TEM) and high-angle annular dark-field scanning TEM (HAADF-STEM). The as-prepared hexagonal nanoplates were the dominant product with monodisperse edge length of around 16 nm and the synthetic yield approaching 100% (Fig. 1, A and B). The thickness of PtPb nanoplates was determined to be 4.5 ± 0.6 nm by analyzing the nanoplates vertical on the TEM grid (Fig. S1). The overall Pt/Pb composition, measured by inductively coupled plasma atomic emission spectroscopy (ICP-AES), was 55.9/44.1 (Pt/Pb), consistent with the TEM energy-dispersive x-ray spectroscopy (TEM-EDX) result (Fig. 1C).

Powder x-ray diffraction (PXRD) pattern of the PtPb nanoplates showed that they were highly crystalline with intermetallic PtPb phase (JCPDS No.06-0374) (Fig. 1D and Fig. S2). The selected-area electron diffraction (SAED) of a single PtPb nanoplate showed its single crystalline and consistent with the diffraction pattern from the [001] zone axis of PtPb (P63/mmc) hexagonal phase (Fig. 1E). However, high-resolution TEM (HRTEM) image of the same nanoplate (Fig. 1F) revealed the edge has a different crystalline structure with the interior. A few edge dislocations were also observed between the edge layer and the interior around the corners, which help to relax the misfit strain between the edge phases. The fast Fourier transform (FFT) patterns indicate a cubic phase at the edge layer and a hexagonal phase of the interior (the insets of Fig. 1F).

The elemental distribution of Pt and Pb at the nanoplates was characterized using STEM-electron energy-loss spectroscopy (EELS) mapping (Fig. 1G), where the Pt (green), Pb (red), and combined (green vs. red) images indeed confirmed the presence of a Pt edge layer around the PtPb core (Fig. 1G). Considering the SAED, HRTEM and the STEM-EELS mapping results together, we can conclude that a Pt shell layer with a cubic phase (Fm-3m) formed at the edge, and the diffraction pattern of Fig. 1E can be interpreted as the overlapped diffraction patterns from the <110> zone axis of strained Pt phase and [001] zone axis of PtPb phase. The Pt shell thickness was determined to be about 0.8 to 1.2 nm (4 to 6 atomic layers).

The abreaction corrected HAADF-STEM imaging technique was further used to characterize the facets and interfaces of the PtPb nanoplates. The nanoplates were imaged from both plate-view and side-view (Fig. 2A). Fig. 2B is a HAADF-STEM image along the PtPb [100] zone axis (side-view) while Fig. 2C is a

HAADF-STEM image from the [001] PtPb zone axis (plane-view). Fig. 2, D to F, are atomic-resolution STEM-HAADF images taken at higher magnifications from the areas indicated by yellow rectangles. The Pt and PtPb phases can be identified from their different stacking sequences. Image simulation with a multisliced method as well as the projection of atoms was overlapped on Fig. 2, D to F. The results confirmed the PtPb(hexagonal)/Pt(cubic) core/shell structure: in addition to the Pt edge layers, there were top (bottom)-Pt layers on the plane surfaces of nanoplates, forming the"perfect"core/shell structure. Thus, two types of interfacial planes formed in PtPb nanoplates, {010}PtPb//{110}Pt between the PtPb and the edge-Pt layer and {001}PtPb//{110}Pt between PtPb and top (bottom)-Pt layer (atomic schematic model of Fig. 2G and Fig. S3-6). Herein, the unique Pt {110} surface would be beneficial for ORR activity enhancement since Pt {110} facet has been demonstrated to be intrinsically more active than Pt {111} facet for the ORR in perchloric acid (24, 25). The SAED, HRTEM and selected-area FFT analysis (Fig. S4-6) further revealed the top-Pt layers were fully coherent to the PtPb core with a 11% compressive strain along the $[01\text{-}1]_{Pt}$ and 7.5% tensile strain along $[100]_{Pt}$, while in the edge-Pt layer, the [001] direction of Pt is fully confined within PtPb, resulting in a 7.5% tensile strain and little compressive strain (1.0%) along [110] Pt (Fig. S3).

The synthesis of 2D pure metal nanoplates is challenging because of the intrinsically isotropic growth behavior of metals (26-28). Time-dependent composition and structure changes revealed that making intermetallic PtPb/Pt core/shell hexagonal nanoplates involved the initial formation of $Pb_3(CO_3)_2(OH)_2$, the transformation of $Pb_3(CO_3)_2(OH)_2$, the reduction of Pt species, and hereafter the interdiffusion to form structurally ordered intermetallic PtPb nanoplates (Fig. S7 and S8). The use of AA as reductant is the key for the formation of well-organized Pt atomic layers because during the synthetic process, AA can work as a weak acid for removing the Pb, allowing the Pt atoms to diffuse and rearrange at higher temperature.

We performed a set of control experiments using a variety of synthetic parameters, such as precursor, surfactant and reducing agent, to investigate how the different synthetic reagents affect the growth of the well-defined PtPb hexagonal nanoplates. The synthesis of well-defined PtPb/Pt nanoplates depended highly on the concentration of Pt and Pb precursors, the combined use of OAm to ODE and the use of proper reducing agents (Fig. S9-15). The concentration of AA also had to stay within a critical range to obtain a high yield of PtPb/Pt core/shell nanoplates (Fig. S14). And also PtPb hexagonal nanoplates could not be made by replacing AA with other reducing agents, such as glucose and citric acid (Fig. S15).

The electrochemical properties of the PtPb nanoplates as well as PtPb nanoparticles that we synthesized (Fig. S16&S17) were studied and further benchmarked against the commercial Pt/C from JM (Pt/C, 20 wt% Pt on Vulcan XC72R carbon, Pt particle size: 2 to 5 nm, Fig. S18A-B). Before the electrochemical measurement, the PtPb nanostructures were uniformly deposited on a commercial carbon (C, Vulcan) support (Fig. S19&S20, named as PtPb nanoplates/C and PtPb nanoparticles/C) via the sonication of PtPb nanostructures and C solution. The products were further treated with the mixture of ethanol/acetic acid to remove the surfactant (29). The inset of Fig. 3A shows cyclic voltammograms (CVs) of PtPb nanoplates/C, PtPb nanoparticles/C and commercial Pt/C catalysts in N_2-purged 0.1 M $HClO_4$ solution at a sweep rate of 50 mV/s. The PtPb nanoplates showed greater electrochemical active surface area (ECSA) of 55.0 m^2/g than PtPb nanoparticles (43.4 m^2/g) because of their thinness and even comparable ECSA to that of the commercial Pt/C (68.9 m^2/g).

To evaluate the electrocatalytic activities toward ORR, the ORR polarization curves of PtPb nanoplates/C, PtPb nanoparticles/C and commercial Pt/C were measured in an O_2-saturated 0.1 M $HClO_4$ solution under Ohmic drop correction (Fig. 3A). As shown in Fig. 3B and Table S1, the specific activity (SA) of PtPb nanoplates/C could reaches 7.8 mA/cm^2 at 0.9 V vs. reversible hydrogen electrode (RHE), 4.1 and 33.9-fold greater than those of PtPb nanoparticles/C (1.9 mA/cm^2) and commercial Pt/C (0.23 mA/cm^2). The mass activity (MA) of PtPb nanoplates/C is 4.3 A/mg$_{Pt}$ at 0.9 V vs. RHE, is ~9.8 times that of 2020 DOE target (30) and places them among the most efficient bimetallic catalysts reported for ORR (8, 21, 22).

The electrochemical durability of the PtPb/Pt core/shell nanoplates was evaluated at the potential between 0.6 and 1.1 V vs. RHE in 0.1 M $HClO_4$ solution. Fig. 3C shows the ORR polarization curves of the PtPb nanoplates/C before and after 10,000, 20,000, 30,000, 40,000, and 50,000 potential cycles. After 50,000 sweeping cycles, there was almost no shift in ORR polarization curves and only 7.7 % loss of mass activity for the PtPb nanoplates (Fig. 3D). However, under the same condition, the PtPb nanoparticles/C showed a large negative shift in ORR polarization curves (Fig. S21A) and 37.0 % loss of mass activity (Fig. 3E). The commercial Pt/C showed a much larger negative shift in ORR polarization curves (Fig. S21B) with 66.7 % loss of mass activity (Fig. 3F). The structures of the catalysts before and after the durability tests were characterized by TEM, SEM-EDX, HRTEM, elemental mappings, and extended X-ray absorption fine structure (EXAFS) (Fig. S19&S22&S23), showing that there was negligible change on the morphology and composition of the PtPb nanoplates (Fig. S19G-I&S22D-F) and Pt-Pt atomic distance (Fig. S23) after long-term cycles. Under the same condition, PtPb nanoparticles show noticeable morphology and composition changes (Fig. S20, C-D) and the commercial Pt/C catalyst exhibited large size changes and substantial aggregation after 50,000 cycles (Fig. S18C-D). We think the high catalytic stability of PtPb/Pt core/shell nanoplates originate from their special structure, in which the well-defined Pt shell can hinder the loss of interior transition metal through the place-exchange mechanism during electrochemical condition and thus significantly improve their ORR durability, which is hardly afforded by the previous reported PtPb/Pt core/shell structures suffering from the typical electrocatalytic activity loss possibly due to their too thin Pt shell (18, 31).

To understand the exceptional ORR performance of the core/shell PtPb/Pt nanoplates, we performed density functional theory (DFT) calculations for the oxygen adsorption energy (E_O) on the PtPb nanoplates. The ORR activity reaches the maximum at some optimal value of E_O (32, 33). For convenience, we shifted the optimal E_O value to 0 eV, and use ΔE_O to represent the difference of a given E_O value relative to this optimal reference. In general, both surface strain and ligand effect can influence the catalytic activity of a core-shell nanostructure, and they can be tuned by the variation of alloy composition in the core. We ignored the ligand effect as it is often negligible for a shell thickness > 0.6 nm (34), and the HRTEM images revealed that the Pt skin thickness is between 0.8 and 1.2 nm, and focus entirely on surface strain.

The SAED and HRTEM results revealed a large tensile strain along [001] and a compressive strain along [110] on both the top-Pt and edge-Pt surfaces of the nanoplates. Thus, we calculated ΔE_O on the Pt (110) surface as a function of strain in the [001] and [110] directions. Specifically, the strain applied in [001] direction ranged from -1% (compressive) to 9% (tensile), and the strain applied in [110] direction varied from 1% to -9%. Under each biaxial strain, three types of most stable oxygen adsorption sites on the (110) surface were examined (Fig. 4A): the face-center cubic (fcc) hollow sites (“h”), the bridge sites in [001] direction (“b1”), and the bridge sites in [110] direction (“b2”). Both “b1” and “b2” sites consist of

the low-coordinated surface atoms. We also calculated ΔE_O on the flat (111) surface of Pt. The results of ΔE_O calculations are reported in Fig. 4, B to D.

The ΔE_O values on the "h" sites were nearly optimal for a wide range of biaxial strains. The adsorbed oxygen atom was metastable when the tensile strain in [001] direction was relatively small or the compressive strain in [110] direction was relatively large. In both cases, the Pt-O binding was much weaker on the "h" sites than their adjacent "b2" sites (Fig. 4, B and D) and the diffusion barrier was < 0.05 eV from an "h" site to a "b2" site. Thus, the "h" sites under such biaxial strains did not contribute meaningfully to the overall ORR. However, under large tensile strain of 7.5% in [001] direction or a small compressive strain of 1% in [110] direction, the "h" sites became catalytically active and their ΔE_O values were comparable to those on the "b2" sites. Thus, the "h" sites on the edge-Pt surface of the nanoplates were stable and active for ORR. The "b1" sites were not active for large tensile strains in [001] direction and was not responsible for the ORR performance of the nanoplates (Fig. 4C). On the "b2" sites, the Pt-O bond was usually strong and could poison the catalyst. However, the strong Pt-O binding could be weakened by tensile strains in [001] direction (Fig. 4D) and the "b2" sites became catalytically active under a large tensile strain of 7.5% in [001] direction.

Because ΔE_O values were insensitive to the strain in [110] direction, the "b2" sites were active for ORR at both the top-Pt and edge-Pt surfaces. We attribute the high ORR activity of the PtPb/Pt core/shell nanoplates to the active "h" and "b2" sites under the appropriate large biaxial strains. It is generally believed that in M/Pt core/shell catalyst, the compressive strain can weaken the Pt-O binding on Pt (111) surface and increase the ORR activity (34-36), and low-coordinated surface atoms have stronger Pt-O binding, lowering the ORR activity (37, 38). However, our DFT calculations show that the tensile strains on Pt (110) facet can also increase the ORR activity and that the low-coordinated surface atoms ("b2") can be activated by large tensile strains.

The ordered PtPb/Pt core/shell nanoplates reported herein also show high electrocatalytic activity and stability toward anodic fuel cell reactions such as methanol oxidation reaction (MOR) and ethanol oxidation reaction (EOR). As shown in Fig. S24-S26&Table S2, the PtPb nanoplates/C exhibits the MOR mass activity of 1.5 A/mgPt, 2.4 times and 7.9 times higher than those of PtPb nanoparticles and Pt catalysts, respectively, as well as higher stability. For EOR, it displays the specific activity of 2.5 mA/cm^2 and mass activity of 1.4 A/mg Pt, 1.9 and 2.5 times greater than those of PtPb nanoparticles/C, and 10.4 times and 8.8 times higher than those of the commercial Pt/C (Fig. S24&Table S3), as well as greater stability (Fig. S24&Fig. S25&Fig. S26).

References and Notes

1. M. Winter, R. J. Brodd, What Are Batteries, Fuel Cells, and Supercapacitors? *Chem. Rev.* **104**, 4245-4269 (2004).

2. A. C. Chen, P. Holt-Hindle, Platinum-Based Nanostructured Materials: Synthesis, Properties, and Applications. *Chem. Rev.* **110**, 3767-3804 (2010).

3. M. S. Dresselhaus, I. L. Thomas, Alternative Energy Technologies. *Nature* **414**, 332-337 (2001).

4. P. Strasser, Catalysts by Platonic Design. *Science* **349**, 379-380 (2015).

5. H. A. Gasteiger, S. S. Kocha, B. Sompalli, F. T. Wagner, Activity Benchmarks and Requirements for Pt, Pt-Alloy, and Non-Pt Oxygen Reduction Catalysts for PEMFCs. *Appl. Catal. B: Environ.* **56**, 9-35 (2005).

6. H. A. Gasteiger, N. M. Marković, Just a Dream-or Future Reality? *Science* **324**, 48-49 (2009).

7. J. K. Nørskov, T. Bligaard, J. Rossmeisl, C. H. Christensen, Towards the Computational Design of Solid Catalysts. *Nat. Chem.* **1**, 37-46 (2009).

8. S. I. Choi, S. F. Xie, M. H. Shao, J. H. Odell, N. Lu, H. C. Peng, L. Protsailo, S. Guerrero, J. Park, X. H. Xia, J. G. Wang, M. J. Kim, Y. N. Xia, Synthesis and Characterization of 9 nm Pt-Ni Octahedra with a Record High Activity of 3.3 A/mg_{Pt} for the Oxygen Reduction Reaction. *Nano Lett.* **13**, 3420-3425 (2013).

9. F. Saleem, Z. C. Zhang, B. Xu, X. B. Xu, P. L. He, X. Wang, Ultrathin Pt-Cu Nanosheets and Nanocones. *J. Am. Chem. Soc.* **135**, 18304-18307 (2013).

10. X. L. Xu, X. Zhang, H. Sun, Y. Yang, X. P. Dai, J. S. Gao, X. Y. Li, P. F. Zhang, H. H. Wang, N. F. Yu, S. G. Sun, Synthesis of Pt-Ni Alloy Nanocrystals with High-Index Facets and Enhanced Electrocatalytic Properties. *Angew. Chem. Int. Ed.* **53**, 12522-12527 (2014).

11. T. Bian, H. Zhang, Y. Y. Jiang, C. H. Jin, J. B. Wu, H. Yang, D. R. Yang, Epitaxial Growth of Twinned Au-Pt Core-Shell Star-Shaped Decahedra as Highly Durable Electrocatalysts. *Nano Lett.* **15**, 7808-7815 (2015).

12. L. Zhang, L. T. Roling, X. Wang, M. Vara, M. F. Chi, J. Y. Liu, S. I. Choi, J. Park, J. A. Herron, Z. X. Xie, M. Mavrikakis, Y. N. Xia, Platinum-Based Nanocages with Subnanometer-Thick Walls and Well-Defined, Controllable Facets. *Science* **349**, 412-416 (2015).

13. C. Wang, M. F. Chi, D. G. Li, D. Strmcnik, D. van der Vliet, G. F. Wang, V. Komanicky, K. C. Chang, A. P. Paulikas, D. Tripkovic, J. Pearson, K. L. More, N. M. Marković, V. R. Stamenkovic, Design and Synthesis of Bimetallic Electrocatalyst with Multilayered Pt-Skin Surfaces. *J. Am. Chem. Soc.* **133**, 14396-14403 (2011).

14. H. Y. Zhu, S. Zhang, S. J. Guo, D. Su, S. H. Sun, Synthetic Control of FePtM Nanorods (M = Cu, Ni) to Enhance the Oxygen Reduction Reaction. *J. Am. Chem. Soc.* **135**, 7130-7133 (2013).

15. J. Zhang, H. Z. Yang, J. Y. Fang, S. Z. Zou, Synthesis and Oxygen Reduction Activity of Shape-Controlled Pt_3Ni Nanopolyhedra. *Nano Lett.* **10**, 638-644 (2010).

16. H. Z. Yang, J. Zhang, K. Sun, S. Z. Zou, J. Y. Fang, Enhancing by Weakening: Electrooxidation of Methanol on Pt_3Co and Pt Nanocubes. *Angew. Chem. Int. Ed.* **49**, 6848-6851 (2010).

17. D. L. Wang, H. L. L. Xin, R. Hovden, H. S. Wang, Y. C. Yu, D. A. Muller, F. J. DiSalvo, H. D.

Abruña, Structurally Ordered Intermetallic Platinum-Cobalt Core-Shell Nanoparticles with Enhanced Activity and Stability as Oxygen Reduction Electrocatalysts. *Nat. Mater.* **12**, 81-87 (2013).

18. T. Ghosh, M. B. Vukmirovic, F. J. DiSalvo, R. R. Adzic, Intermetallics as Novel Supports for Pt Monolayer O_2 Reduction Electrocatalysts: Potential for Significantly Improving Properties. *J. Am. Chem. Soc.* **132**, 906-907 (2010).

19. J. Greeley, I. E. L. Stephens, A. S. Bondarenko, T. P. Johansson, H. A. Hansen, T. F. Jaramillo, J. Rossmeisl, I. Chorkendorff, J. K. Nørskov, Alloys of Platinum and Early Transition Metals as Oxygen Reduction Electrocatalysts. *Nat. Chem.* **1**, 552-556 (2009).

20. M. F. Francis, W. A. Curtin, Mechanical Work Makes Important Contributions to Surface Chemistry at Steps. *Nat. Commun.* **6**, 6261 (2015).

21. C. Chen, Y. J. Kang, Z. Y. Huo, Z. W. Zhu, W. Y. Huang, H. L. L. Xin, J. D. Snyder, D. G. Li, J. A. Herron, M. Mavrikakis, M. F. Chi, K. L. More, Y. D. Li, N. M. Marković, G. A. Somorjai, P. D. Yang, V. R. Stamenkovic, Highly Crystalline Multimetallic Nanoframes with Three-Dimensional Electrocatalytic Surfaces. *Science* **343**, 1339-1343 (2014).

22. X. Q. Huang, Z. P. Zhao, L. Cao, Y. Chen, E. B. Zhu, Z. Y. Lin, M. F. Li, A. M. Yan, A. Zettl, Y. M. Wang, X. F. Duan, T. Mueller, Y. Huang, High-Performance Transition Metal–Doped Pt_3Ni Octahedra for Oxygen Reduction Reaction. *Science* **348**, 1230-1234 (2015).

23. See the supplementary materials on *Science* Online.

24. N. M. Marković, R. R. Adžić, B. D. Cahan, E. B. Yeager, Structural Effects in Electrocatalysis: Oxygen Reduction on Platinum Low Index Single-Crystal Surfaces in Perchloric Acid Solutions. *J. Electroanal. Chem.* **377**, 249-259 (1994).

25. M. D. Maciá, J. M. Campiña, E. Herrero, J. M. Feliu, On the Kinetics of Oxygen Reduction on Platinum Stepped Surfaces in Acidic Media. *J. Electroanal. Chem.* **564**, 141-150 (2004).

26. X. Q. Huang, S. H. Tang, X. L. Mu, Y. Dai, G. X. Chen, Z. Y. Zhou, F. X. Ruan, Z. L. Yang, N. F. Zheng, Freestanding Palladium Nanosheets with Plasmonic and Catalytic Properties. *Nat. Nanotechnol.* **6**, 28-32 (2011).

27. X. H. Xia, J. Zeng, Q. Zhang, C. H. Moran, Y. N. Xia, Recent Developments in Shape-Controlled Synthesis of Silver Nanocrystals. *J. Phys. Chem. C* **116**, 21647-21656 (2012).

28. L. Chen, F. Ji, Y. Xu, L. He, Y. F. Mi, F. Bao, B. Q. Sun, X. H. Zhang, Q. Zhang, High-Yield Seedless Synthesis of Triangular Gold Nanoplates through Oxidative Etching. *Nano Lett.* **14**, 7201-7206 (2014).

29. V. Mazumder, S. H. Sun, Oleylamine-Mediated Synthesis of Pd Nanoparticles for Catalytic Formic Acid Oxidation. *J. Am. Chem. Soc.* **131**, 4588-4589 (2009).

30. U.S. Department of Energy, Technical Plan: Fuel Cells, **2016**, (http://www.energy.gov/sites/prod/files/2016/06/f32/fcto_myrdd_fuel_cells_0.pdf).

31. C. Roychowdhury, F. Matsumoto, V. B. Zeldovich, S. C. Warren, P. F. Mutolo, M. Ballesteros, U. Wiesner, H. D. Abruña, F. J. DiSalvo, Synthesis, Characterization, and Electrocatalytic Activity of PtBi and PtPb Nanoparticles Prepared by Borohydride Reduction in Methanol. *Chem. Mater.* **18**, 3365-3372 (2006).

32. J. K. Nørskov, J. Rossmeisl, A. Logadottir, L. Lindqvist, Origin of the Overpotential for Oxygen Reduction at a Fuel-Cell Cathode. *J. Phys. Chem. B* **108**, 17886-17892 (2004).

33. V. Stamenkovic, B. S. Mun, K. J. J. Mayrhofer, P. N. Ross, N. M. Marković, J. Rossmeisl, J. Greeley, J. K. Nørskov, Changing the Activity of Electrocatalysts for Oxygen Reduction by Tuning the Surface Electronic Structure. *Angew. Chem., Int. Ed.* **45**, 2897-2901 (2006).

34. X. Zhang, G. Lu, Computational Design of Core/Shell Nanoparticles for Oxygen Reduction Reactions. *J. Phys. Chem. Lett.* **5**, 292-297 (2014).

35. M. Mavrikakis, B. Hammer, J. K. Nørskov, Effect of Strain on the Reactivity of Metal Surfaces. *Phys. Rev. Lett.* **81**, 2819-2822 (1998).

36. P. Strasser, S. Koh, T. Anniyev, J. Greeley, K. More, C. F. Yu, Z. C. Liu, S. Kaya, D. Nordlund, H. Ogasawara, M. F. Toney, A. Nilsson, Lattice-Strain Control of the Activity in Dealloyed Core–Shell Fuel Cell Catalysts. *Nat. Chem.* 2, 454-460 (2010).

37. L. Li, A. H. Larsen, N. A. Romero, V. A. Morozov, C. Glinsvad, F. Abild-Pedersen, J. Greeley, K. W. Jacobsen, J. K. Nørskov, Investigation of Catalytic Finite-Size-Effects of Platinum Metal Clusters. *J. Phys. Chem. Lett.* **4**, 222-226 (2013).

38. D. F. van der Vliet, C. Wang, D. Tripkovic, D. Strmcnik, X. F. Zhang, M. K. Debe, R. T. Atanasoski, N. M. Marković, V. R. Stamenkovic, Mesostructured Thin Films as Electrocatalysts with Tunable Composition and Surface Morphology. *Nat. Mater.* **11**, 1051-1058 (2012).

Acknowledgement

This work was financially supported by the National Key Research and Development Program of China (No. 2016YFB0100201), the National Natural Science Foundation of China (21571135 and 51671003), the Ministry of Science and Technology (2016YFA0204100), the start-up fundings from Soochow University and Peking University, Young Thousand Talented Program and the Priority Academic Program Development of Jiangsu Higher Education Institutions (PAPD). Part of electron microscopy work was performed at the Center for Functional Nanomaterials, Brookhaven National Laboratory, which is supported by the U.S. Department of Energy (DOE), Office of Basic Energy Science, under Contract No. DE-SC0012704. The work at California State University Northridge was supported by the US Army

Research Office via the MURI grant W911NF-11-1-0353. We thank Shaobo Cheng for his help in the simulation of STEM imaging. **All data are reported in the main text and supplement.**

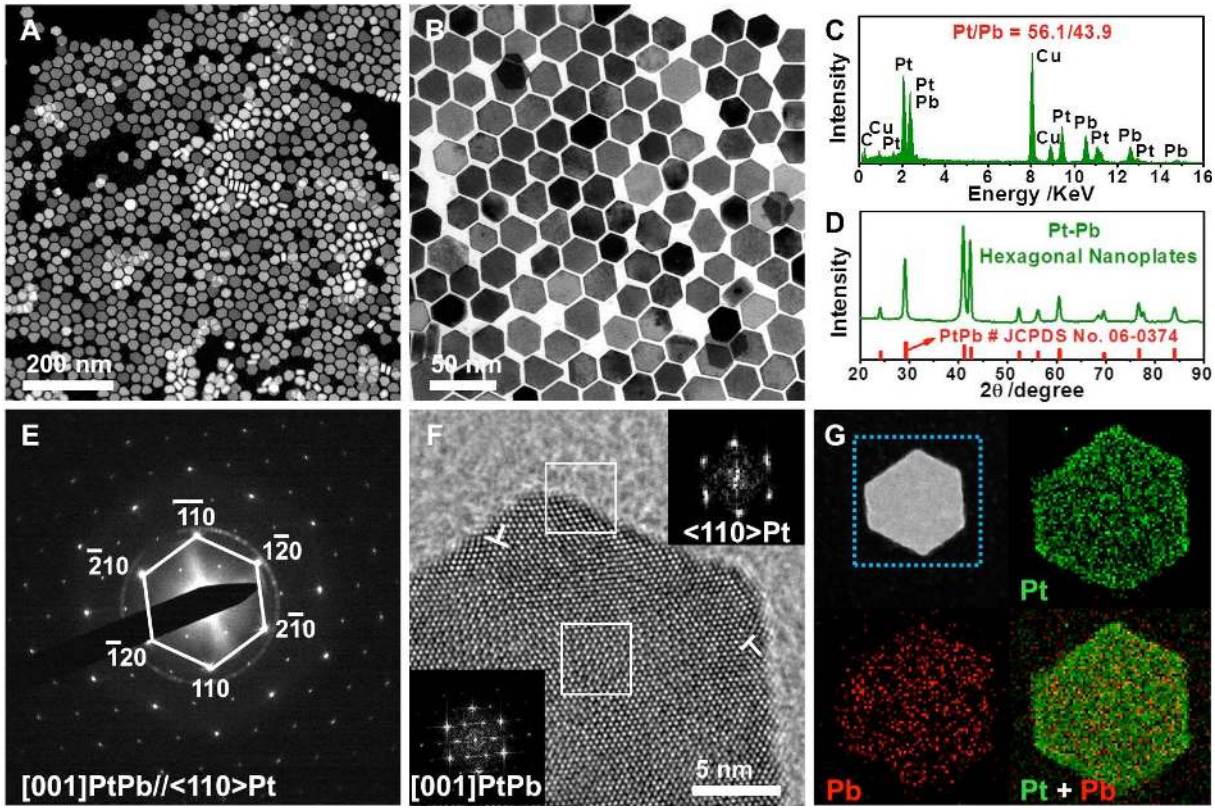

Fig. 1. Morphology and Structure Characterization of PtPb Hexagonal Nanoplates. Representative (A) HAADF-STEM image, (B) TEM image, (C) TEM-EDX and (D) PXRD pattern of PtPb hexagonal nanoplates. (E) SAED and (F) HRTEM of one single hexagonal nanoplate. Insets of Fig. 1F are the FFT patterns from the white squares at the edge of and inside the nanoplate, respectively. (G) STEM-EELS elemental mapping of PtPb hexagonal nanoplates: HAADF-STEM image, Pt mapping in green, Pb mapping in red, and integrated mapping of Pt and Pb are shown. The compositional ratio between Pt/Pb is 55.9/44.1, as revealed by ICP-AES.

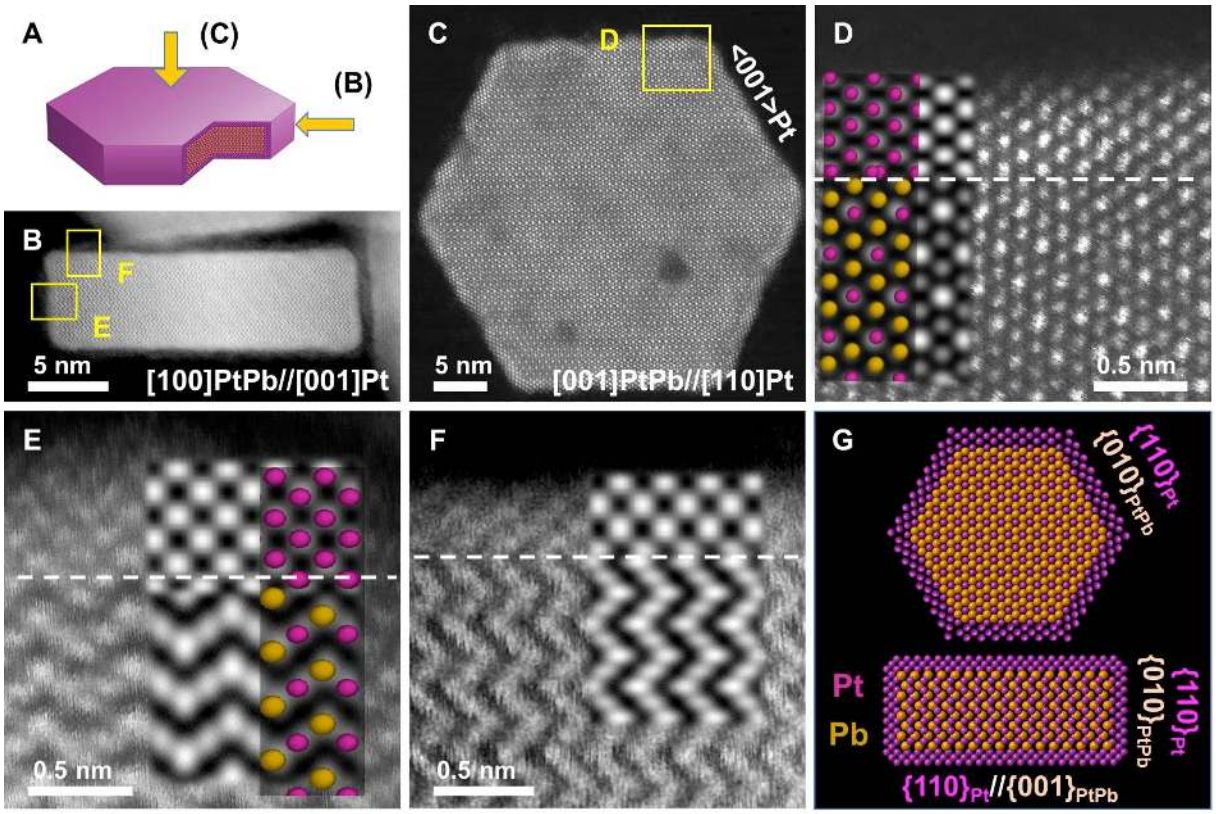

Fig. 2. Structure Analysis of PtPb Nanoplates. (A) A model of one single hexagonal nanoplate, (B) HAADF-STEM image from in-plate view, (C) HAADF-STEM image from out-of-plate view. (D), (E), and (F) are high-resolution HAADF images from the selected areas in (C) and (B) respectively. Simulated HAADF images as well as the atomic models are superimposed on the experimental images. (G) The schematic atom models of the nanoplate showing the top interface ((110)Pt//(100)PtPb and side interface (110)Pt//(001)PtPb, along [100] zone axis of PtPb.

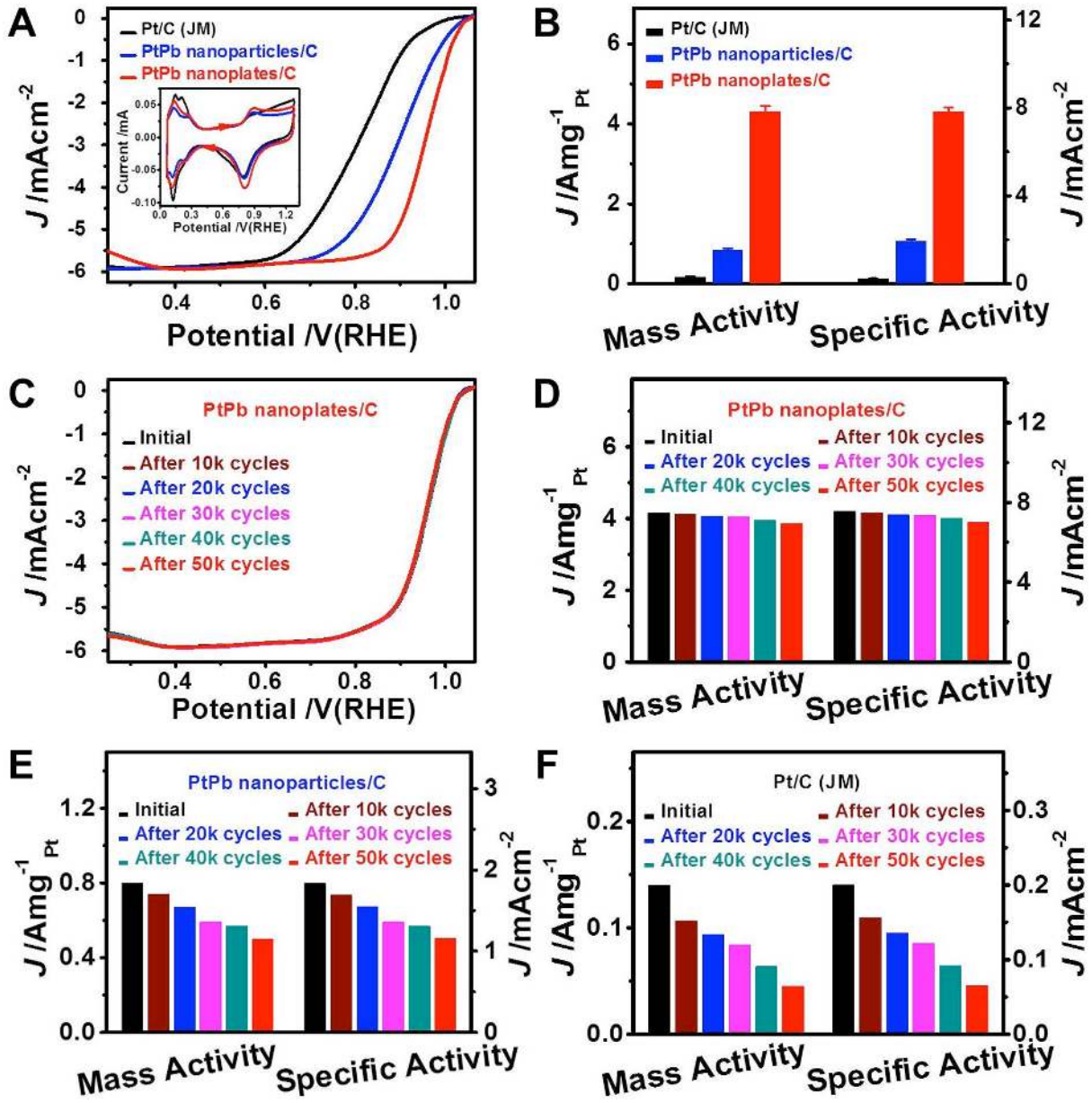

Fig. 3. Electrocatalytic Performance of PtPb Nanoplates/C, PtPb Nanoparticles/C and Commercial Pt/C Catalysts for ORR. (A) ORR polarization curves and (B) specific activities and mass activities of different catalysts. Inset in (A) is the CVs of different catalysts in 0.1 M $HClO_4$ solution at a sweep rate of 50 mV/s. The ORR polarization curves were recorded at room temperature in an O_2-saturated 0.1 M $HClO_4$ aqueous solution. The activities were calculated based on five parallel measurements after Ohmic drop correction. (C) ORR polarization curves of the PtPb nanoplates/C catalyst before and after different potential cycles between 0.6-1.1 V vs. RHE. (D) The changes on specific and mass activities of the PtPb nanoplates/C catalyst before and after different potential cycles. (E) The changes on specific and mass activities of the PtPb nanoparticles/C catalyst before and after different potential cycles. (F) The changes on specific activities and mass activities of the commercial Pt/C catalyst before and after different potential cycles.

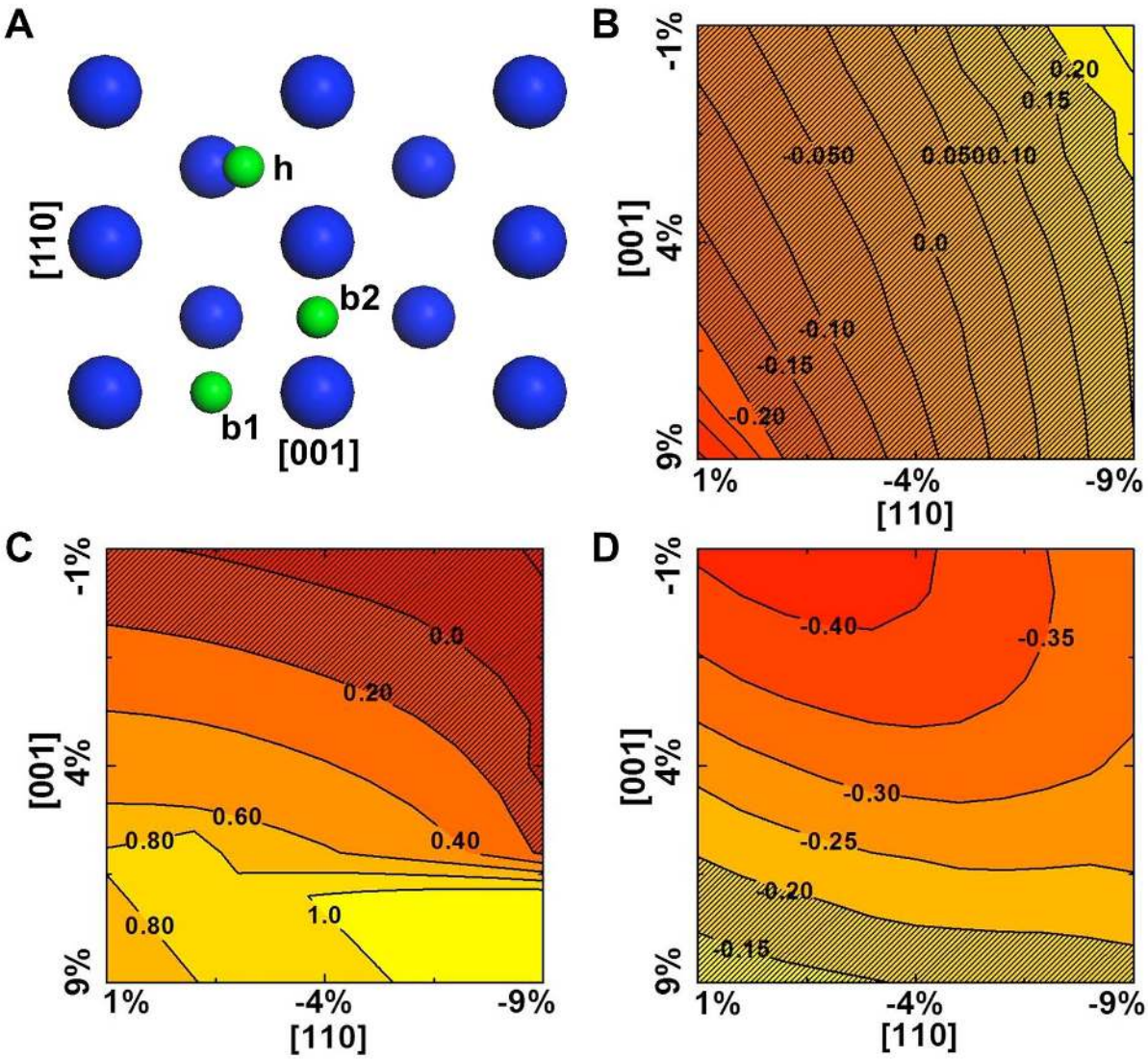

Fig. 4. DFT Calculations of Oxygen Adsorption Energy. (A) Atomic models of the Pt (110) surface. Three stable adsorption sites for oxygen: hollow ("h") and two bridge sites ("b1" and "b2"). The blue and green spheres represent Pt and O atoms, respectively. On the Pt (110) surface, ΔE_O as a function of biaxial strain in [110] and [001] directions for the "h" site (B), "b1" site (C) and "b2" site is plotted in (D). The optimal ΔE_O value is set to be 0. ΔE_O value falling into the shaded region implies a higher ORR activity than that on the flat Pt (111) surface.